Paper-Like 100% Si Nanowires Electrodes Integrated with Argyrodite Li$_6$PS$_5$Cl Solid Electrolyte

Elena Sánchez-Ahijón,[a, b] Afshin Pendashteh,*[a] and Juan J. Vilatela*[a]

Silicon anodes are a promising solution in all-solid-state batteries (ASSBs) due to minor lithium dendrite risk, high capacity, and low potential. Research on Si integration in ASSBs is still nascent, requiring a deep understanding of the interplay between electrode composition, structure, and performance. Here, we present the first study on 100% Si nanowires integrated with Li$_6$PS$_5$Cl solid electrolyte (SE). The anodes are paper-like networks of aggregated Si nanowires produced by a slurry-free method without carbon/binders. Despite the lack of any conductor, the Si anodes provide > 2.5 Ah/g capacity at a high mass loading of 1.7 mg/cm^2(~5 mAh/cm^2), demonstrating sufficient electric and ionic conductivities. Electro-chemo-mechanical properties of the electrodes over (de)lithiation were

probed through electrochemical impedance spectroscopy, ex-situ microscopy, and in-operando pressure regulation measurements. The lithiated electrode/SE interface was found to be electrochemically stable. Cross-sectional microscopy at various states-of-charge confirmed the buffering effect of the anode porosity, resulting in the preservation of the electrode's thickness after the first lithiation but a considerable shrinkage during delithiation, producing cracking and formation of the new interface. Capacity remains constant for five cycles, then decreases linearly up to 40 cycles. This is attributed to repeated fracture of the anode/electrolyte interface and the corresponding impedance increase.

Introduction

All-solid-state batteries (ASSBs) are considered promising alternatives to conventional Li-ion batteries (LIBs) due to their projected higher safety and energy density. Silicon (Si) has recently been attracting attention as an alternative anode (e.g., to Li metal) in ASSBs due to its high theoretical capacity (e.g., 3579 mAh/g), comparable cost, better interfacial compatibility with solid-electrolytes (SE), processability, etc.,[1,2] In addition, Si anodes are less prone to dendrite growth risk during charge and void formation during discharge compared to Li metal. Nevertheless, large volume changes and morphological transformation of Si and its corresponding chemo-mechanical impact on the battery performance in the confined solid-state environment have yet to be understood and addressed.

Early reports on solid-state Si electrodes were focused on thin film anodes and oxide-based ceramic electrolytes.[3,4] The development of sulfide-based fast ionic conductors (e.g., > 1 mS/cm) and the fact that the projected enhanced energy of the ASSBs is achievable only with thick electrodes (e.g., ≥ 7 mAh/cm^2) have recently stimulated more research efforts on the integration of high Si content electrodes (e.g., ≥ 1 mg$_{Si}$/cm^2) with sulfide-based SEs.[5] Evidently, Li diffusivity and lithiation propagation in solid-state Si electrodes depend

strongly on compositional and morphological aspects (e.g., the size, shape, and aspect ratio) of the particles and their interactions with other electrode components (e.g., SE and conducting additives, if any). *Tan et al.* reported successful integration of Si microparticles with Li$_6$PS$_5$Cl (LPSCl) argyrodite SE, showcasing long cycle life (e.g., 500 cycles with a capacity retention of 80%) when paired with LiNi$_{0.8}$Mn$_{0.2}$Co$_{0.2}$O$_2$ (a.k.a., NMC-811) cathode composites.[6] The excellent performance was attributed to a stable two-dimensional (2D) Si|SE interface. In addition, they observed a detrimental effect of carbon additives on electrolyte decomposition. In another study, *Huo et al.* contrasted the chemo-mechanical failure mechanisms between pure Si and Si/SE composite electrodes.[7] Accordingly, more extended SEI growth at the Si|SE interface was observed in the composite electrodes. *Cao et al.* correlated the electrochemical properties of Si electrodes with the macroscopic stacking pressure, revealing the impact of the pressure on lithiation homogeneity.[8] Very recently, *Cao et al.* studied the mechanical and electrochemical evolution of nano-Si composite anodes based on the premise that nano-Si exhibits higher structural stability and fewer void formations because of their smaller size, which can potentially relieve the stresses.[9]

While these investigations provide significant insight into the electrochemical properties of solid-state Si electrodes, the use of alloying anodes in ASSBs is still nascent, requiring a better understanding of their charge storage and failure mechanisms as well as their correlation with compositional/microstructural properties of the Si electrode. There are few studies on nanoscale Si integrated with sulfide-based electrolytes and even fewer studies on 1D particles with high aspect ratios.[9–14] This is while Si nanowires (Si NWs) exhibited great opportunities in conventional LIBs due to their unique properties, including short Li$^+$ diffusion paths, anisotropic stress

[a] E. Sánchez-Ahijón, A. Pendashteh, J. J. Vilatela
IMDEA Materials Institute, Eric Kandel 2, Getafe, Madrid, 28906, Spain
E-mail: afshin.pendashteh@imdea.org
juanjose.vilatela@imdea.org

[b] E. Sánchez-Ahijón
Department of Applied Physics, Universidad Autónoma de Madrid, Francisco Tomás y Valiente 7, 28049 Cantoblanco, Madrid, Spain

Batteries & Supercaps

Research Article
doi.org/10.1002/batt.202400292

Chemistry Europe
European Chemical
Societies Publishing

distribution, resistance to pulverization, and thus improved cycling properties.[15–17] In a recent study, *Grandjean et al.* compared the integration of Si microparticles and Si NWs composite electrodes with various sulfide-based SEs. They found that the Si NW composite electrode performed better in cyclability. However, it is noted that the electrodes in these studies are mostly composites with polymeric and/or carbon additives, compromising the overall electrode capacity and possibly affecting the electrochemical signal.

To contribute to the understating of the alloying reaction in ASSBs, here we introduce another model system comprising 100% Si NWs with reproducible, well-defined microstructure and bulk properties. The electrodes are entirely made of Si with virtually unlimited thickness, fabricated via continuous Si NW direct assembly from the gas phase and are free of any binder or conducting agent.[17] Herein, we study such electrodes as an excellent model system in combination with LPSCl argyrodite SE. The electrochemical properties of the electrodes are measured via different techniques, including galvanostatic charge-discharge measurements, differential capacity analysis, and electrochemical impedance spectroscopy. Accordingly, the Si NW electrodes displayed a high reversible capacity of over 2400 mAh/g, good initial coulombic efficiency (e.g., ICE = 77%), and a high average CE of 97.5% over cycling. In addition, the morphological evolution (e.g., porosity) of the Si NWs was monitored during the cell stacking procedure and consecutive (de)lithiation, suggesting that (i) the Si NWs are preserved over cycling, (ii) the electrode porosity can absorb the expansion during first lithiation, and (iii) the electrode shrinkage in the course of delithiation causes formation of cracks at the electrode/electrolyte interface as well as microscale vertical cracks within the electrode layer which are responsible of the electrode polarization and capacity fading. To the best of our knowledge, this is the first study of pure Si NW electrodes with practical mass loadings with a SE. This work not only presents the electrochemical properties of such electrodes in combination with a sulfide-based inorganic electrolyte but also sheds some light on their possible failure mechanisms, which could potentially guide further improvements of solid-state Si electrodes.

Experimental/Methods

Synthesis of Si Nanowire Paper-like Electrodes

The Si NW anodes (Si:Coil®) were supplied by Floatech. Details of the synthesis of the self-standing Si NW fabrics can be found in our earlier published work.[18] Briefly, Si NW fabrics were produced using floating catalyst chemical vapor deposition (FCCVD) in which a continuous aerosol of Si NWs is formed in the gas phase when gold nanoparticles as the catalyst meet with the gaseous precursor (SiH_4) in the hot reaction zone (e.g., 650 °C) of a vertical reactor. The crystallinity of the Si NWs was >95% when the reaction was conducted in a H_2 atmosphere.[19] The intertwined nanowires in the form of fabrics were collected on porous filter membranes, peeled off as self-standing samples (similar to non-woven fabrics), and transferred/calendered on commercial copper foils (e.g., as current

collectors). The anodes consist of 99.7 vol.% Si. Unless otherwise specified, the areal mass of the Si NW anodes was 0.9 mg/cm².

Physicochemical Characterizations

Morphological aspects of the samples were probed using Field Emission Scanning Electron Microscopy (FESEM, FEI Helios NanoLab 600i simultaneously acquiring images using TLD and CBS detectors) at an accelerated voltage of 5 kV and Energy Dispersive Spectroscopy (EDS). The cross-sectional imaging was conducted using a Focused Ion Beam (FIB) and a Ga source. Raman spectra were collected using a Renishaw spectrometer (equipped with 532 nm, Green) on pristine and cycled electrodes with 5% power, 5 *s* of exposure time, and 25 accumulations. Electrical conductivity measurements were conducted using a Keithley SourceMeter (model 2450).

Electrochemical Measurements

The Si NW electrodes were dried (e.g., to remove any physiosorbed moisture) before assembly at 80 °C under vacuum overnight. All electrode and electrolyte preparations and cell assemblies were carried out in a glove box with a controlled inert atmosphere (i.e., $H_2O < 0.3$ ppm, $O_2 < 0.1$ ppm). The electrochemical properties of the Si NWs as alloying electrodes were studied in a two-electrode configuration against a mixture of the InLi (e.g., $Li_{0.8}In$)[20] intermetallic alloy with the SE serving as the counter electrode. The stable and representative potential of the counter electrode and sufficient Li reservoir is ensured using $Li_{0.8}In$ composition. The InLi alloy was simply prepared by consecutive folding/laminating of the corresponding metallic foils with an appropriate mass ratio (i.e., Li:In of 95.4:4.6) until achieving a matte and fragile powder. Lithium Phosphorus Sulfur Chloride (LPSCl, NEI corporation, US) was employed as the SE. A self-standing SE layer was prepared by mechanical pressing (e.g., at room temperature) of a known amount of the SE within a commercial cell (Sphere Energy, ASC–A) in which the internal pressure can be adjusted through a set of screws and using calibrated torque wrenches. Accordingly, the SE layer was formed with a pressure of 167 MPa over 5 min. The typical thickness of the SE layers was ~300 μm. The InLi alloy powder was mixed with the SE in a mass ratio of InLi:SE of 60:40 and pressed against the preformed SE layer from the previous step at a stacking pressure of 137 MPa for 5 min. Finally, the half-cell was completed by adding the Si NW working electrode (circle-shaped electrodes with a diameter of 6 mm) and the cell was hermetically sealed at a stacking pressure of 82 MPa. The cells were electrochemically probed by galvanostatic cycling at C/20 (e.g., 1 C = 3.579 A/g as for $Li_{15}Si_4$)[21] with an upper voltage cut-off of 1.5 V and a lower cut-off of 0.01 V vs. Li/Li⁺. All electrochemical potentials depicted in this work were converted from In/InLi to Li/Li⁺ using $E_{Li/Li^+} = E_{In/InLi} + 0.6$.[22] In-operando pressure measurements were made using a CompeCell 12PEEK DP together with Compre-Frame cell stand (rhd instruments GmbH) with 30 kN spring, 10 kN sensor, and at temperature equilibrating at 25 °C. The cycling procedure started after 12 hours of initial rest time.

Results and Discussions

The electrodes employed in this work are comprised of self-standing, flexible sheets made entirely of Si NWs fabricated through a novel route based on FCCVD.[18] Long Si NWs (c.a., 2.5 μm) with an ultra-fast growth rate (c.a., >1.4 μm/s) are formed in a gas stream arising from the rapid mixing of

Batteries & Supercaps

Research Article
doi.org/10.1002/batt.202400292

Chemistry Europe
European Chemical
Societies Publishing

reactants. Because of their high aspect ratio (e.g., $L/\phi \approx 180$), the nanowires entangle and form a macroscopic freestanding sheet without needing binders, polymers, or any reprocessing whatsoever. The Si NW nanotextiles, as densified, are flexible paper-like sheets (see Figure 1a) that are simply turned into finished battery electrodes after being calendered on the copper current collector, as seen in Figure 1b. This assembly route circumvents slurry processing, eliminating the need for solvents, dispersants, mixing, casting, drying, etc., which aligns with the demands of ASSB manufacture. In addition, the mechanical stability of the Si NW network enables handling as regular paper and ensures that the electrode withstands the pressure required for ASSB assembly, as shown below.

Microstructurally, the anode is composed of a dense network of aggregated crystalline Si NWs with almost isotropic pore structure (e.g., BET surface area of ~54 m^2/g for the as-prepared Si NWs) originated from imperfect packing of the nanowires. The high porosity of the Si NW paper electrodes can
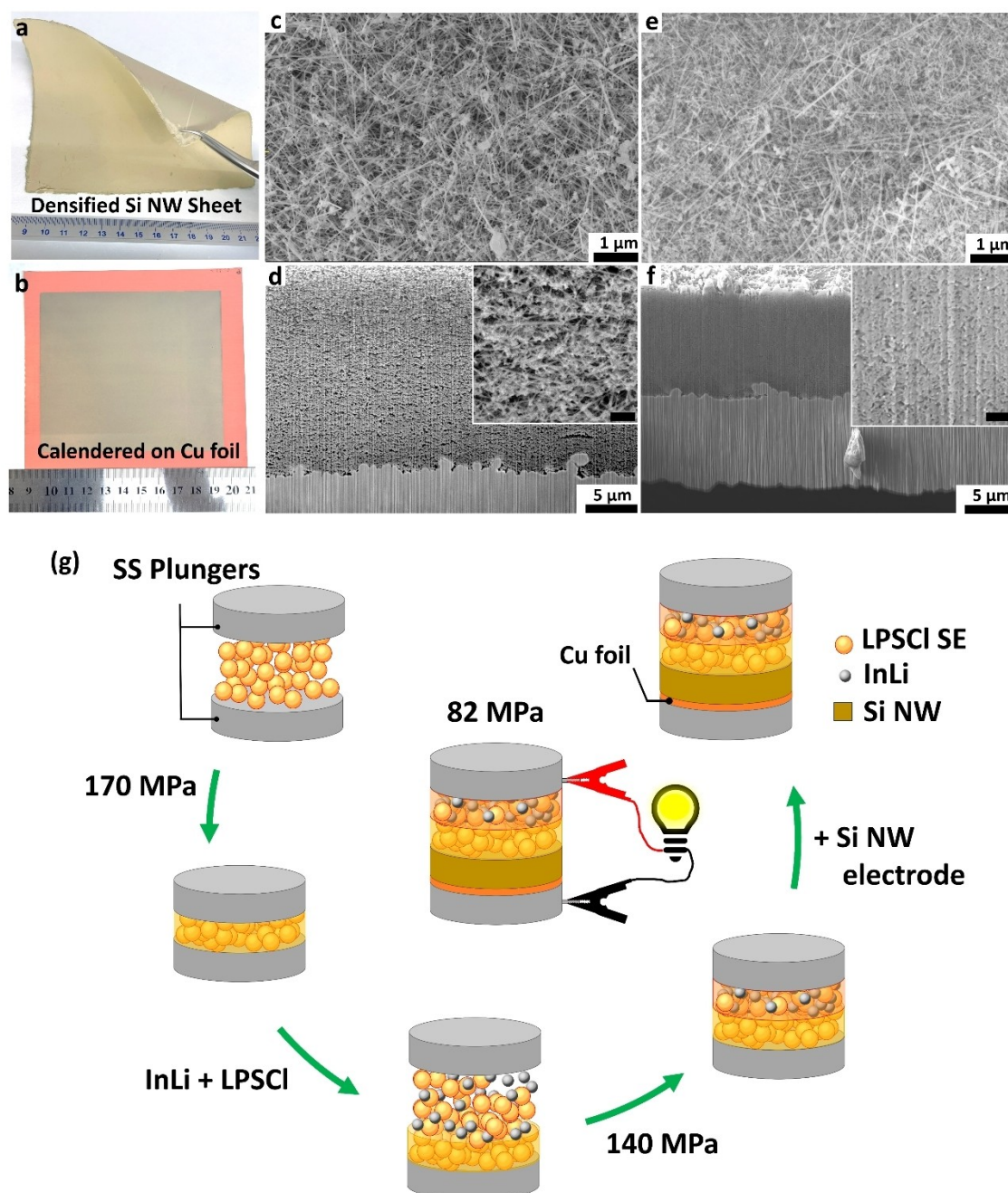

Figure 1. Si NW nanotextile anode produced via FCCVD. Digital photographs of the Si NW nanotextile electrodes (a, b) with 10 cm×10 cm dimension in various states: (a) densified forming a self-standing, flexible sheet, and (b) calendered on Cu foil as the current collector. Field emission SEM micrographs of the surface of Si NW nanotextile electrodes as calendered (c) and after cell assembly (e), along with their corresponding cross-sectional micrographs (d and f, respectively) obtained by FIB-SEM. The inset micrographs show magnified cross-section of the electrodes, and the scale bar is equal to 500 nm. Panel (g) displays schematic representation of various steps followed to assemble the all-solid-state half-cells tested in the present work.

Batteries & Supercaps

Research Article
doi.org/10.1002/batt.202400292

Chemistry Europe
European Chemical
Societies Publishing

be realized from the surface and cross-sectional SEM micrographs (see Figure 1c, d and Figure S1) and is estimated at $>85\%$ based on the electrode's dimensions (i.e., electrode geometrical area and the estimated average thickness of $\sim 24\ \mu m$ from FIB-SEM and optical micrographs, see Figure S1 and S2). The Si NW electrodes are entirely made of crystalline Si (with only 0.3 vol.% of residual Au catalyst), and their dimensions, mass loading, porosity, etc., can be readily tunned during the fabrication process, thus making excellent model systems whose study can help decouple interlinked electro-chemo-mechanical processes in solid-state electrochemical cells.

When assembled in a solid-state cell under high stack pressure (i.e., 82 MPa, see the scheme in Figure 1g), the Si NW paper electrodes retained their morphological structure (see Figures 1e, f, and S3), although their porosity is reduced as the result of mechanical compaction (c.a., average thickness of 9.5 μm and average porosity of ~63%). Under the applied stacking pressure, the porous Si NW reaches a limiting density

as densification increases stiffness and approaches that of the Si crystal.

LPSCl was employed as the SE due to its high ionic conductivity (e.g., 3 mS/cm)[23] and reported good stability against Si-based electrodes.[13] The electrochemical signature of the 100% Si NW paper-like electrodes (Figure 2a) displays a first lithiation capacity of over 3765 mAh/g, of which a high reversible capacity of ~2650 mAh/g (i.e., ICE of 70%) is achieved during the first delithiation. Notably, such high reversible capacity is comparable with the one achieved in conventional liquid electrolyte (e.g., 2741 mAh/g, see Figure S4), demonstrating that the Si NW paper anodes possess sufficient electric and ionic conductivities to attain high specific capacity in solid-state (e.g., in the absence of an impregnating electrolyte or conducting additives, Si NWs are the only charge carrier pathway through the electrode layer). It is noted that the Si NW electrodes are SE-free, and no apparent mixing of the Si NWs with SE particles was observed from SEM images (e.g., in Figure 1e and f), which is expected due to large SE particles
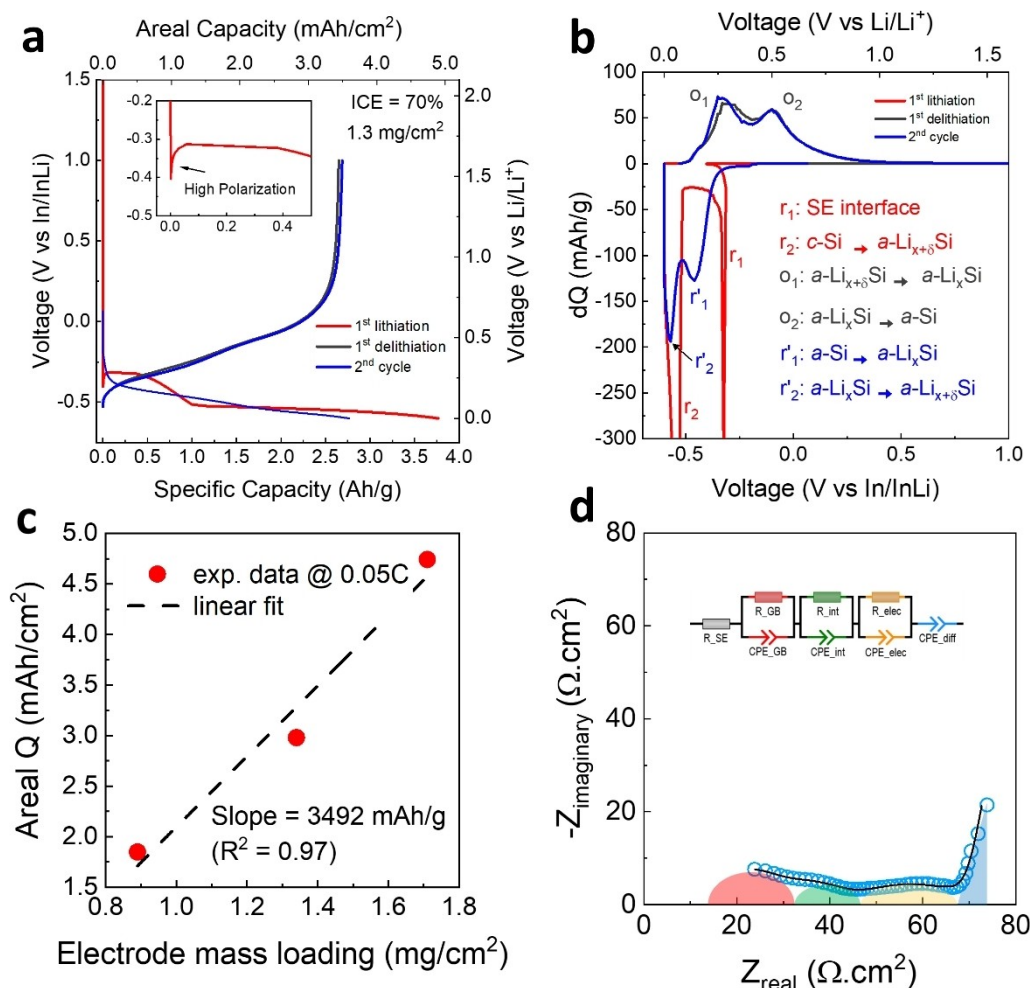

Figure 2. Electrochemical properties of the Si NW nanotextile anodes in integration with LPSCl SE. (a) The first two voltage profiles of the Si NW paper anodes in an In/InLi∣LPSCl∣Si NW configuration at 0.05 C rate (1 C = 3.579 A/g). The inset magnifies the first lithiation, highlighting the initial high polarization. (b) The corresponding differential capacity curves over the first two cycles, together with the possible reaction assignments. (c) The Si NWs paper anodes' areal capacity with various areal masses (e.g., thicknesses) suggests a linear relationship. (d) Typical impedance (e.g., Nyquist plot) of the Si NW nanotextile electrodes observed after the first lithiation. The inset displays the equivalent circuit employed to fit the experimental data (shown as empty circles). The solid line shows the fitted data, and the components are shown in color shades for better representation.

(c.a., 2 μm, see Figure S5). The relatively soft LPSCl provides good and close contact with the Si NW layer after pressing at 82 MPa. As seen, the first lithiation voltage profile displays a high initial overpotential (see the inset in Figure 2a) down to ~−0.4 V (vs. In/InLi), which is attributed to the sluggish ion diffusion and electron transfer in the crystalline Si (c-Si) anode. This is later followed by two plateaus, the first one appearing as a hump (~−0.32 V vs In/InLi) and the second plateau at lower voltage (c.a., $-0.52\,V \approx 0.1\,V$ vs Li/Li$^+$). The second more pronounced plateau suggests the existence of both c-Si and amorphous Si (a-Si) phases (e.g., two-phase field reaction) over most of the alloying reaction. The low reduction potential (e.g., $E_{r2} \sim -0.52$ vs In/InLi) during the Si matrix amorphization likely originated from the large activation energy needed to break the Si−Si bonds in c−Si. This could be further realized by the disappearance of the c-Si Raman bands after cycling (see Figure S6). One immediate difference between the electrochemical response of the Si NW electrode cycled in solid-state with the one cycled in the conventional liquid electrolyte is the absence of the c-Li$_{15}$Si$_4$ distinctive peak during delithiation (at ≈ 0.45 V vs Li/Li$^+$), suggesting that the lithiation depth in the solid-state electrolyte is more likely below $x = 3.75$ (in Li$_x$Si). In the second cycle, the lithiation voltage profile is significantly altered, converting to a sloping plateau, while the second delithiation is nearly identical to that of the first cycle. This is attributed to the fact that the c−Si is amorphized during the first lithiation and is not crystalized in the subsequent delithiation, just like in the liquid system. As is seen in Figure 2b, a pair of reduction and oxidation peaks appeared after the second cycle, corresponding to consecutive reversible conversion of a−Si to a−Li$_x$Si ($x \approx 2$) and a−Li$_{x+\delta}$Si. Further in-situ characterizations are required to illuminate the exact reaction mechanism and intermediate compositions of Si anodes in solid-state cells. As expected, the polarization and peak separation are increased (i.e., reduction peaks towards more negative potentials and oxidation peaks shift in the opposite direction) in the solid-state cell compared to that of the liquid cell (see Table S1) as a result of increased reaction activation energies and reduced reaction reversibility in the solid-state.

When tested with different mass loadings of Si NW paper-like anodes (i.e., various electrode thickness), the areal capacity of the electrode is scaled linearly (see Figure 2c), achieving a high, application-relevant areal capacity of 4.7 mAh/cm^2. Linear fitting of the experimental data, achieving a specific capacity of 3490 mAh/g ($R^2 = 97$), reveals near-theoretical capacity accessible for relatively thick electrodes at 0.05 C rate. This clearly demonstrates that the lithiation reaction occurs through the thickness of the pure Si NW anodes (e.g., in the absence of any conducting or binding additive) even at high mass loadings, suggesting that the pure Si anode can provide mixed conductivity (i.e., both ionic and electronic) as soon as a small amount of Li is introduced during the lithiation. Such good performance in pure Si electrodes without any conducting additive is attributed to the network structure of the Si nanotextile, formed by a dense ensemble of nanowires with high aspect ratio particles increasing the interconnection within

the electrode. This could be further realized through an out-of-plane conductivity of ~0.6 mS/m, which is in the range of intrinsic crystalline silicon.[24,25]

To further investigate the alloying reaction as well as the interface between the Si NW paper anode and LPSCl SE, electrochemical impedance spectroscopy (EIS) was conducted. Figure 2d shows the Nyquist plot of the cell in fully lithiated condition and after reaching the steady state, along with the equivalent circuit used for fitting. It should be noted that a simplified model is used as Si acts as both the ionic and electric ionic path in the absence of SE or conducting agents within the Si NW electrode layer. As is seen, the spectrum comprises three suppressed semicircles at the high-mid frequency region, and a linear tail at low-frequencies. These are modeled by three (RQ) loops in series (e.g., Q stands for constant phase element), representing the ion transport resistance in the SE separator (e.g., grain boundary resistance), the combined LPSCl|Si NW and InLi|LPSCl interfaces' resistance (e.g., R_int), and the electrode charge transfer contribution, respectively. The linear slope at lower frequencies (e.g., < 0.5 Hz) is attributed to diffusion polarization. The diffusion coefficient of the Li$^+$ ion (D_{Li}^+) was estimated as 2.4×10^{-13} cm^2/s, comparable to those reported for solid-state Si electrodes.[26] To study the stability of the LPSCl|Si NW interface, further EIS measurements were carried out every hour for 20 h (see Figure S7) after the first lithiation. No significant change was observed in the Nyquist plot of the cell over a period of 20 h, revealing that the interface between the lithiated Si NWs and the LPSCl is stable (i.e., LPSCl|Li$_x$Si). This observation is contrary to that seen in composite electrodes consisting of Si microparticles and SE particles.[7] The difference might be attributed to the nanoscale Si particles employed in the current work, which can potentially improve the distribution of the stack pressure to the electrode layer and, hence, more homogeneous lithiation of the Si particles in the adjacent with the SE separator, resulting in a more (electro)chemically stable 2D interface.[8]

We then carried out ex-situ SEM analysis of electrode cross-sections, which provides direct insight not only into the microstructure of the Si NW anode over (de)lithiation but also the evolution of internal pressure in the cell. Figure 3 shows examples of the Si NW anode and part of the 2D interface with the electrolyte at full lithiated and delithiated states over the first cycle. The thickness of the electrode hardly changes under full lithiation (see Figure 3c). This is expected, given the high porosity of the anode. Porosity is 63% when measured ex-situ but likely very similar under pressure inside the cell. The electrode is an aerogel of entangled nanowires whose compressive modulus increases rapidly with increasing density. Indeed, the anode under full lithiation still shows around 40% porosity. These observations confirm that full lithiation is possible without significant anode expansion.

Surprisingly, upon delithiation, anode thickness drops abruptly, reducing apparent porosity to less than 5% (see Figure 4c). After the first cycle, the anode transforms into a compact layer of highly aggregated Si NWs (Figure 3f). However, the nanowires could still be recognized in the electrode (see Figure 4a, b), suggesting that the nanowires do not
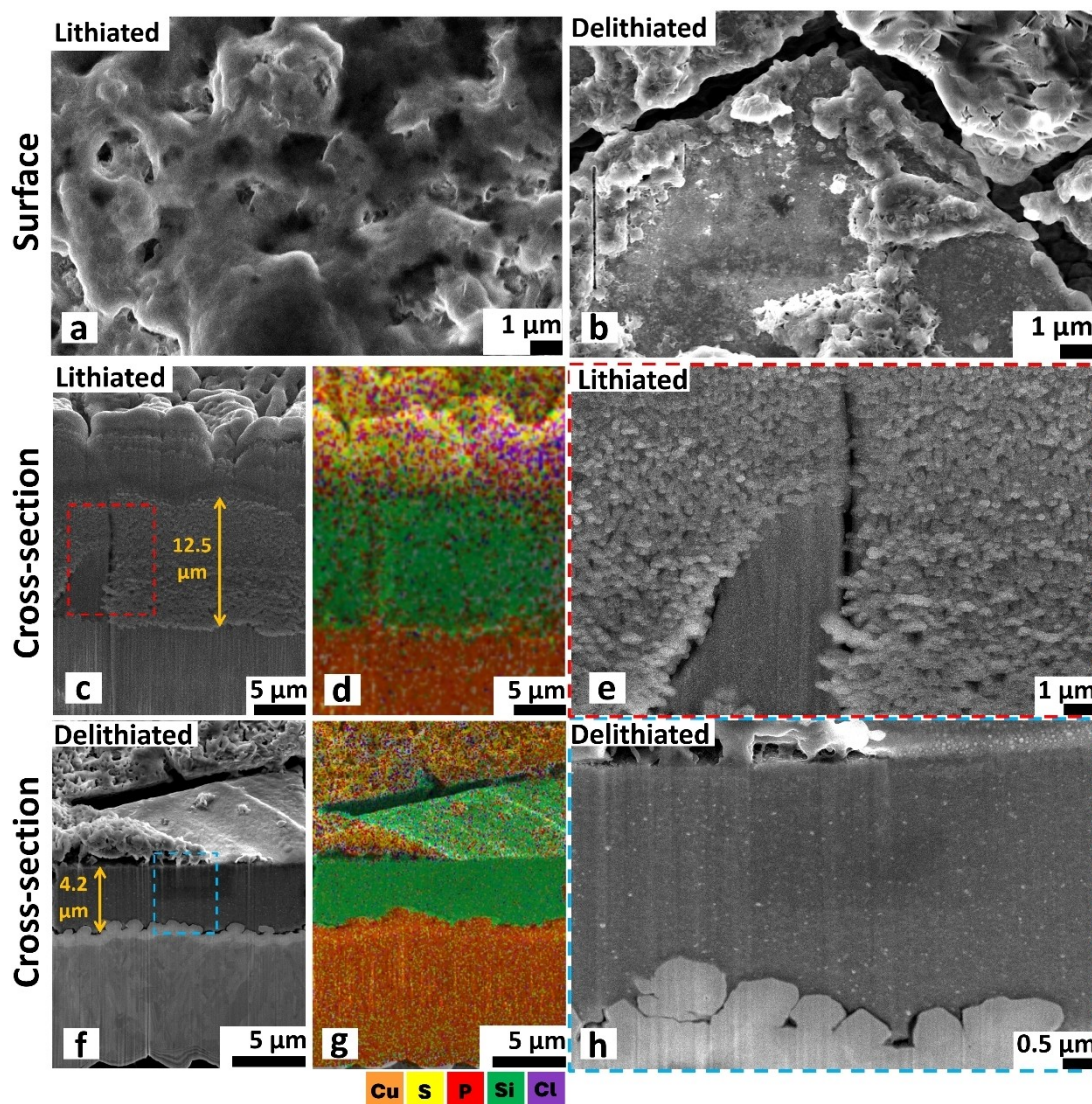
Figure 3. Morphological evolution of the pure Si NW paper anodes over lithiation and delithiation in In/InLi│LPSCl│Si NW cell. SEM micrographs of the surface of the Si NW electrode after (a) lithiation and (b) delithiation. Cross-sectional micrographs of the Si NW paper anodes collected using FIB in the lithiated (c, e) and delithiated (f, h) states, together with their corresponding EDX elemental mapping (d and g, respectively).

coalesce. Densification during de-lithiation occurs through compaction of the nanowire network, which is enabled by the reduction in nanowire bending modulus upon amorphization, nanowire shortening, and possibly a reduction in shear stress transmission during Li diffusion.

Due to the changes in electrode morphology during the first delithiation, in subsequent electrochemical cycles, the evolution of internal pressure and electrode response will differ from that in the first cycle. Whereas in the first cycle, the anode is thick and porous and does not expand substantially, in subsequent cycles, it is thin and would expand significantly. This is indeed what is observed when using a dedicated in-operando cell with a pressure gauge (see Figure S9). The second and following cycles show an increase in pressure during lithiation and a decrease during de-lithiation. The first cycle shows more pressure events arising from internal changes in the cell layers. A sudden pressure drop immediately starting

during the first delithiation is marked and associated with anode densification.

A detailed description of cell pressure based on the mechanical properties of the cell layers is complicated by the coupling of the degree of lithiation, electrode thickness, and electrode modulus[7] and is beyond the scope of this work. However, we can estimate that the changes in initial compressive stress arising from changes in anode thickness (Δh) between cycles are of the order of $\Delta\sigma = \frac{\Delta h}{A} k$, where A is the electrode area and k is the spring constant of the spring commonly used in dedicated cells for ASSBs.[27] The resulting stress difference is only ≈ 10 kPa. This implies that the largest effect of anode shrinkage is not in the dimensional change of the cell and the resulting pressure exerted but in the change of anode microstructure and the interface with the SE, and their response upon lithiation/delithiation.
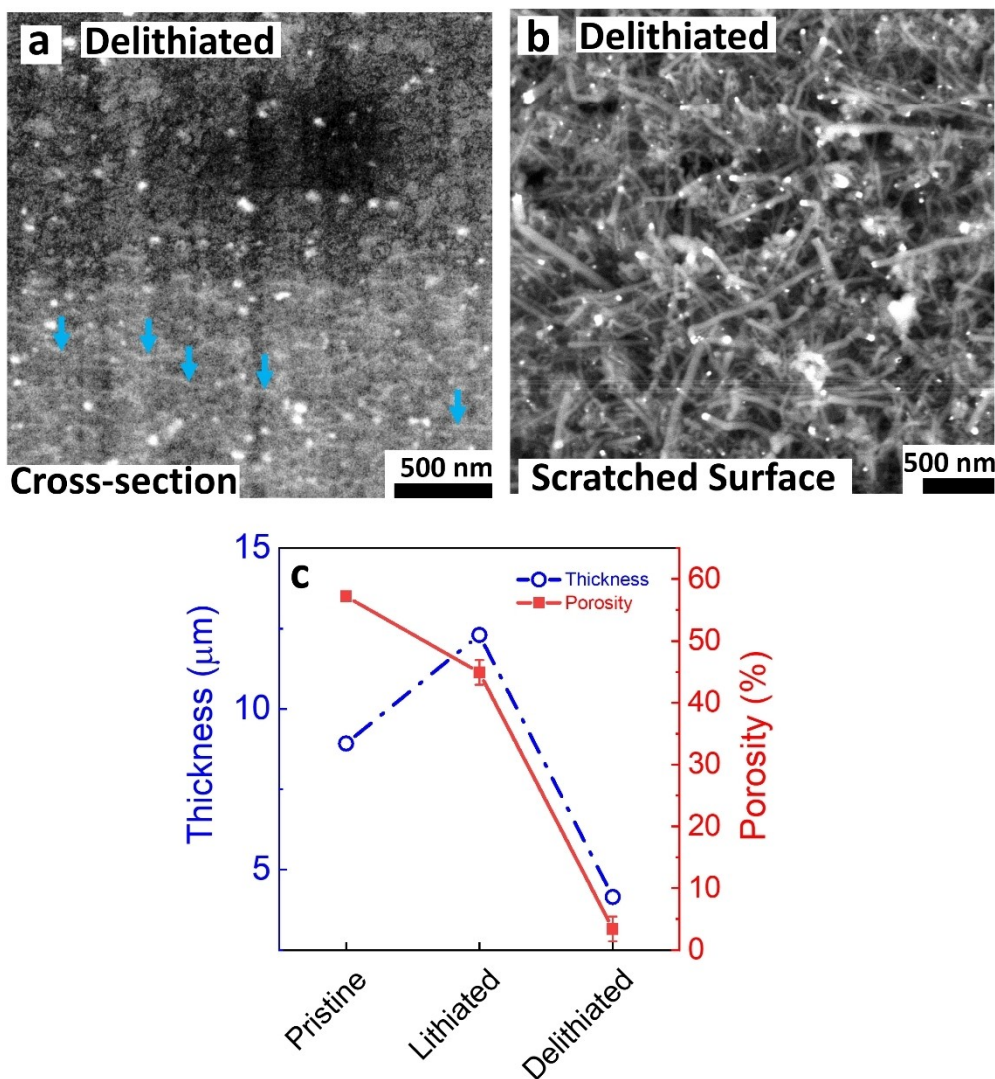
Figure 4. Microstructure evolution of Si NW paper anodes over cycling. High magnified cross-sectional micrograph of the Si NW paper anode after delithiation (a). The Si NWs still can be identified and are marked with light blue arrows. The micrograph of the delithiated sample after mechanical removal of its surface. The nanowires are readily seen, confirming that the wires are not fused together during lithiation. The electrode thickness evolution (e.g., obtained from FIB-SEM measurements) as well as its corresponding estimated porosity over the first cycle is plotted in panel (c).

The question then moves onto cyclability. Figure 5a depicts the capacity retention of the Si NW paper anodes in half-cell over the first 35 cycles. It is seen that the capacity is stable for the initial 5 cycles (apart from the loss in the first cycle due to SEI formation), but then it starts to decrease gradually with a nearly linear behavior. Impedance measurements after nine cycles (see Figure 5b and Table S2) show that the main increased resistance is related to the interface component. This finding is in agreement with the observed changes in the mechanical properties of the electrode after initial cycles, where the abrupt loss of the electrode porosity after the first delithiation stimulates mechanical stresses on the electrode/SE interface in the following cycles, resulting in cracking of the 2D interface (see Figure 6a, b). In addition, vertical microvoids could also be observed in the electrode layer (marked with red arrows). In contrast, the interface between the Si electrode and the current collector appeared intact even after delithiation.

This suggests good adhesion of the Si NW layer to the current collector. The compressive strain generated during delithiation and the good adhesion of the electrode layer to the current collector could describe the appearance of the vertical micro voids within the electrode layer. The proposed capacity fading mechanism is schematically shown in Figure 6c. Accordingly, the main reasons for capacity fading are the abrupt volume shrinkage of the Si NW electrodes after the first delithiation and the consequential loss of electrode porosity. Hence, the overall cycling properties could be potentially improved by mitigating the electrode shrinkage (e.g., by reinforcing the Si NW electrode microstructure) after the first delithiation.
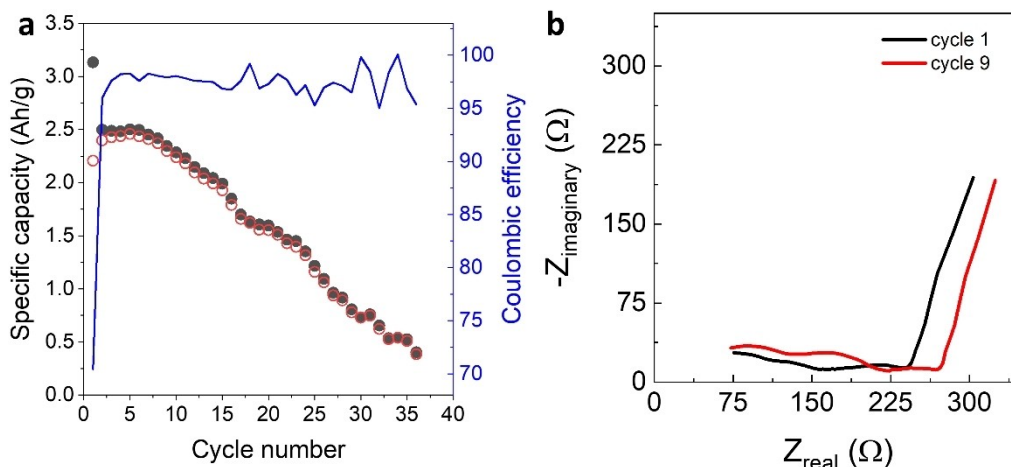
Figure 5. Cycling properties of the Si NW nanotextile paper anodes in integration with LPSCl SE. (a) The evolution of specific (dis)charge capacities over cycling in In/InLi│LPSCl│Si MW cell at 0.05 C rate. (b) The comparison of the EIS data before and after cycling.
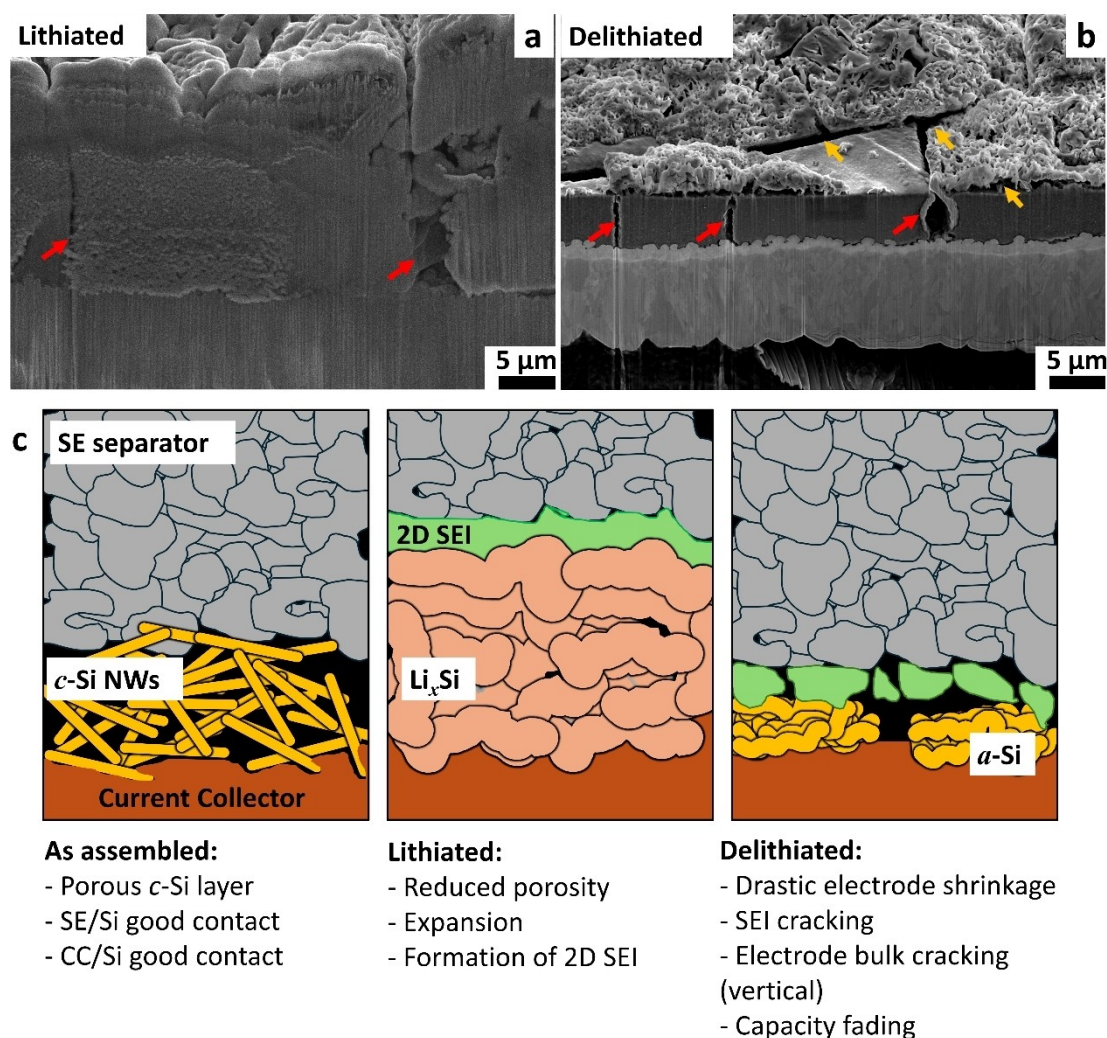

Figure 6. Microstructural evolution over cycling and possible failure mechanism. The FIB cross-sectional micrograph of the lithiated (a) and delithiated (b) Si NW paper anode. The vertical cracks in the electrode bulk layer are shown with red arrows and the ones on the surface with yellow arrows. Schematic representation of the microstructural evolution of the Si NW electrodes over (de)lithiation in which the drastic shrinkage of the electrode over delithtaion and formation of cracks result in electrode capacity fading.

Conclusions

In summary, the electrochemical behavior of the 100% Si NWs paper anodes in integration with LPSCl solid electrolyte was extensively studied, and their electro-chemo-mechanical evolution was tracked through ex-situ post-mortem microscopy, impedance spectroscopy, and in-operando pressure control measurements. The Si NW electrodes showed a high specific capacity of over 2.5 Ah/g, even at relatively high mass loadings, suggesting sufficient mixed ionic and electric conductivities. According to the obtained results, the abrupt electrode volume shrinkage over the first delithiation and its following mechanical stress on the electrode/electrolyte interface, together with the altered volume change pattern during the subsequent cycles, are found to be responsible for the capacity fading of the electrode.

Author Contributions

E.S.A. performed the investigation, visualization, validation, and reviewed and edited the final manuscript. A.P. performed conceptualization, methodology, investigation, visualization, validation, supervision, funding acquisition, wrote the original draft, and reviewed and edited the final manuscript. J.J.V. performed conceptualization, supervision, funding acquisition, and reviewed and edited the final manuscript.

Acknowledgements

Conflict of Interests

J.J.V. has a financial interest in Floatech, which commercializes Si NW anodes.

Data Availability Statement

The data that support the findings of this study are available from the corresponding author upon reasonable request.

[1] J. A. Lewis, K. A. Cavallaro, Y. Liu, M. T. McDowell, *Joule* **2022**, *6*, 1418.
[2] J. Janek, W. G. Zeier, *Nat. Energy* **2023**, *8*, 230.
[3] B. P. H. L. Notten, F. Roozeboom, R. A. H. Niessen, L. Baggetto, *Adv. Mater.* **2007**, *19*, 4564.
[4] V. P. Phan, B. Pecquenard, F. Le Cras, *Adv. Funct. Mater.* **2012**, *22*, 2580.
[5] D. Cao, X. Sun, Y. Li, A. Anderson, W. Lu, H. Zhu, *Adv. Mater.* **2022**, *34*, 2200401.
[6] D. H. S. Tan, Y.-T. Chen, H. Yang, W. Bao, B. Sreenarayanan, J.-M. Doux, W. Li, B. Lu, S.-Y. Ham, B. Sayahpour, J. Scharf, E. A. Wu, G. Deysher, H. Eun Han, H. Jin Hah, H. Jeong, B. Lee Jeong, Z. Chen, Y. S. Meng, *Science* **2021**, *373*, 1494.
[7] H. Huo, M. Jiang, Y. Bai, S. Ahmed, K. Volz, H. Hartmann, A. Henss, C. V. Singh, D. Raabe, J. Janek, *Nat. Mater.* **2024**, *23*, 543.
[8] Q. Cao, Z. Sun, K. Ye, P. Shen, K. Jiang, S. Bo, *Energy Storage Mater.* **2024**, *67*, 103246.
[9] D. Cao, T. Ji, A. Singh, S. Bak, Y. Du, X. Xiao, *Adv. Energy Mater.* **2023**, *13*, 2203969.
[10] W. Yan, Z. Mu, Z. Wang, Y. Huang, D. Wu, P. Lu, J. Lu, J. Xu, Y. Wu, T. Ma, *Nat. Energy* **2023**, *8*, 800.
[11] M. Yamamoto, M. Takatsu, R. Okuno, A. Kato, M. Takahashi, *Sci. Rep.* **2023**, *13*, 17051.
[12] J. Trevey, J. S. Jang, Y. S. Jung, C. R. Stoldt, S. Lee, *Electrochem. Commun.* **2009**, *11*, 1830.
[13] M. Grandjean, M. Pichardo, Y. Biecher, C. Haon, P. Chenevier, *J. Power Sources* **2023**, *580*, 233386.
[14] M. Rana, Y. Rudel, P. Heuer, E. Schlautmann, C. Rosenbach, Y. Ali, H. Wiggers, A. Bielefeld, W. G. Zeier, *ACS Energy Lett.* **2023**, *8*, 3196.
[15] C. K. Chan, H. Peng, G. Liu, K. McIlwrath, X. F. Zhang, R. A. Huggins, Y. Cui, *Nat. Nanotechnol.* **2008**, *3*, 31.
[16] M. Rana, A. Pendashteh, R. S. Schäufele, J. Gispert, J. J. Vilatela, *Adv. Energy Mater.* **2022**, *12*, 2103469.
[17] A. Pendashteh, R. Tomey, J. J. Vilatela, *Adv. Energy Mater.* **2024**, *14*, 2304018.
[18] R. S. Schäufele, M. Vazquez-Pufleau, J. J. Vilatela, *Mater. Horiz.* **2020**, *7*, 2978.
[19] R. S. Schäufele, M. Vazquez-Pufleau, A. Pendashteh, J. J. Vilatela, *Nanoscale* **2022**, *14*, 55.
[20] B. Hennequart, M. Deschamps, R. Chometon, B. Leube, R. Dugas, E. Quemin, P. Cabelguen, C. Lethien, J. Tarascon, *ACS Appl. Energ. Mater.* **2023**, *6*, 8521.
[21] M. N. Obrovac, L. Christensen, *Electrochem. Solid-State Lett.* **2004**, *7*, A93.
[22] A. L. Santhosha, L. Medenbach, J. R. Buchheim, P. Adelhelm, *Batteries & Supercaps* **2019**, *2*, 524.
[23] C. N. Shuo Wang, Y. Zhang, X. Zhang, T. Liu, Y. Lin, Y. Shen, L. Li, *ACS Appl. Mater. Interfaces* **2018**, *10*, 42279.
[24] E. H. Putley, W. H. Mitchell, *Proc. Phys. Soc.* **1958**, *72*, 193.
[25] M. Khardani, M. Bouaïcha, W. Dimassi, M. Zribi, S. Aouida, B. Bessaïs, *Thin Solid Films* **2006**, *495*, 243.
[26] X. Xu, Q. Sun, Y. Li, F. Ji, J. Cheng, H. Zhang, Z. Zeng, Y. Rao, H. Liu, D. Li, L. Ci, *Small* **2023**, *19*, 2302934.
[27] C. Lee, J. Y. Kim, K. Y. Bae, T. Kim, S. J. Jung, S. Son, H. W. Lee, *Energy Storage Mater.* **2024**, *66*, 103196.